Analyzing Interfacial Transport for Water Evaporating into Dry Nitrogen

Brandon Murray, Matthew J. Fox, Shankar Narayan*

Department of Mechanical, Aerospace, and Nuclear Engineering, Rensselaer Polytechnic Institute, 110 8th Street, Troy, NY 12180

*Corresponding author. E-mail address: narays5@rpi.edu. Telephone: 1-518-276-6988

Abstract

Designing air-water systems for industrial applications requires a fundamental understanding of mass accommodation at the liquid-vapor interface, which depends on many factors, including temperature, vapor concentration, and impurities that vary with time. Hence, understanding how mass accommodation changes over a droplet's lifespan is critical for predicting the performance of applications leveraging evaporation. In this study, experimental data of water droplets on a gold-coated surface evaporating into dry nitrogen is coupled with a computational model to measure the accommodation coefficient at the liquid-vapor interface. We conduct this measurement by combining macroscopic observations with the microscopic kinetic theory of gasses. The experiments utilize a sensitive piezoelectric device to determine the droplet radius with high accuracy and imaging to measure the droplet contact angle. This setup also quantifies the trace amounts of non-volatile impurities in the droplet. For water droplets evaporating in a pure nitrogen stream, the accommodation coefficient directly relates to vapor flux over the droplet's surface and is affected by the presence of impurities. We obtained a surfaceaveraged accommodation coefficient close to 0.001 across multiple water droplets evaporating close to room temperature. This quantification can aid in conducting a more accurate analysis of evaporation, which can assist in the improved design of evaporation-based applications. We believe the modeling approach presented in this work, which integrates the kinetic theory of gases to the macroscale flow behavior, can provide a basis for predicting evaporation kinetics in the presence of extremely dry non-condensable gas streams.

Keywords: accommodation coefficient; droplet evaporation; interfacial transport; evaporation kinetics;

1 Introduction

The evaporation of water in dry air is a commonly occurring phenomenon in nature and industrial applications. Hence, droplet evaporation has undergone extensive investigation for more than a century, beginning with Maxwell's¹ and Langmuir's² pioneering works. Nevertheless, there is continued interest in evaporation for its role in applications such as fuel combustion,^{3–5} microfluidics,^{6,7} desalination,⁸ inkjet printing,⁹ spray cooling, fire suppression,¹⁰ and DNA synthesis.¹¹ Particularly, evaporative cooling^{12–19} has gained significant interest in recent years for managing heat in various applications. However, enabling high flux evaporation requires a fundamental understanding, especially for determining the rate-limiting transport mechanism, which in many cases can be the transport across the liquid-vapor interface.

One of the critical unknown parameters in calculating the transport across the liquid-vapor interface is the mass accommodation coefficient (AC), which controls evaporation kinetics. In general, prior experiments have shown that ACs for non-polar substances are close to unity. At the same time, ACs for water can span orders of magnitude from 0.001 to 1, as noted by multiple authors. ^{20–23} The reasons attributed to this wide range in AC often include varying definitions of ACs, ²⁴ experimental conditions and procedures, and dissolved impurities. ^{20,21,25} Also, it is challenging to determine the physical quantities necessary to quantify AC, such as pressure ²⁰ and temperature ²⁶ near the interface. ²⁶ This challenge is often addressed by data extrapolation. ²⁰ While these issues can result in the inaccurate prediction of evaporation and a wide range of AC, accounting for the presence of non-condensable gas during evaporation introduces more challenges.

Like single-component systems, multi-component systems, such as air-water, are common in many industrial applications. For example, air-liquid binary systems are relevant in electronic cooling,⁵⁵ water desalination,⁵⁶ climate control,^{57,58} and water harvesting systems.⁵⁹ However, the theoretical framework for single-component systems does not hold for binary systems, wherein one of the components could be non-condensable. In this

regard, prior studies have considered Ar/Ne mixtures using molecular dynamics, 50,60,61 and other gas mixtures by direct numerical simulation $^{49,62-64}$ and theoretical analysis. $^{65-67}$ Recent work by Ohashi *et al.* 62 investigates higher pressures non-condensable gases in a two-component system of equal size and mass. It shows the vaporizing component's AC to decrease to $\sigma = 0.1$ with increasing non-condensable concentration, which aligns with trends observed in experiments. 20,21,68 Indeed, in all prior studies, the AC was found to decrease with increasing non-condensable gas concentration. While most efforts consider comparable vapor and non-condensable gas mole fractions, water evaporation in dry air represents an extreme case of relatively low vapor mole fractions (~ 0.03). Our study addresses this extreme case to facilitate accurate modeling of similar operating conditions.

For water evaporating in dry air, heat and mass transfer phenomena are inherently inseparable. The conduction and convection of heat and vapor diffusion in the ambient can all play significant roles. Besides geometric factors, ambient conditions, and other parameters, 5,27,28 self-cooling during evaporation can cause a temperature gradient leading to surface tension-driven Marangoni flows. While computational modeling can account for many of these accurately, 29–34,35–41 the primary unknown remains to be the treatment of transport across the liquid-vapor interface. This work investigates this aspect by considering the evaporation of water droplets in a non-condensable gas (nitrogen) atmosphere.

This study describes a theoretical model to quantify evaporation flux at the liquid-vapor interface when water droplets evaporate in a dry environment. We also determine the AC for water by coupling experiments with numerical modeling. As the AC depends on interfacial conditions such as temperature, impurities, and ambient vapor concentration, it can change during evaporation due to self-cooling of the droplet, accumulation of impurities, and changes in the surrounding gas. We quantify these changes during evaporation for determining the AC accurately. The theoretical model described in this study and the AC measured for water evaporating in dry nitrogen can help predict evaporation in similar systems without performing exhaustive experiments and computational modeling. We demonstrate this by comparing our model predictions with experiments in different settings. Since water evaporation in dry air is a ubiquitous phenomenon and crucial in several industrial applications, the theoretical model and the AC determined in this study can be used as an interface condition in computational models to predict performance accurately.

1.1 Theoretical Model for Evaporation of Binary Systems

At the microscale, the Knudsen layer is the non-equilibrium gas region near the interface.⁴² This layer, typically described using the Boltzmann transport equation, ^{43–49} controls the interfacial transport of molecules from the liquid to the vapor phase. Other approaches to analyze this region to quantify interfacial transport includes statistical rate theory²⁵ and molecular dynamics. ^{24,42,50–54}

In this study, we extend the theory of single component evaporation (Eq. (2)) to analyze multi-component evaporation. Hertz⁶⁹ and Knudsen⁷⁰ provide the evaporation rate of mercury in vacuum based on the equation commonly known as the Hertz-Knudsen Equation.

$$\dot{m}^{"} = \sqrt{\frac{m}{2\pi k_B}} \left(\sigma_e \frac{p_s(T_l)}{\sqrt{T_l}} - \sigma_c \frac{p_v}{\sqrt{T_v}} \right) \tag{1}$$

Here \dot{m}'' is the mass flux, m is the mass of a single molecule, k_B is the Boltzmann constant, σ_e and σ_c are the evaporation and condensation coefficients, T_l is the liquid temperature, T_v is the vapor temperature at the edge of the Knudsen layer, $p_s(T_l)$ is the saturation pressure evaluated at the liquid interfacial temperature and p_v is the vapor pressure evaluated at the edge of the Knudsen layer. Figure 1(a) shows the location of p_s , T_l , p_v and T_v relative to the liquid-vapor interface and Knudsen layer. It is essential to note that while σ_e and σ_c is not specified independently in several studies, a common simplification of $\sigma_e = \sigma_c = \sigma$ is often made. $\sigma_e^{(20,43,71)}$

Eq. (1) does not include the evaporation flux's effect on the velocity distribution near the liquid-vapor interface. Since this effect is not negligible, Schrage⁴³ derived Eq. (2).

$$\dot{m}^{"} = \sigma \sqrt{\frac{m}{2\pi k_B}} \left(\frac{p_s(T_l)}{\sqrt{T_l}} - \frac{p_v}{\sqrt{T_v}} \Gamma(\phi_v) \right) \tag{2}$$

$$\Gamma(\phi) = e^{-\phi^2} - \phi\sqrt{\pi}(1 - \operatorname{erf}(\phi)) \tag{3}$$

Here σ is the accommodation coefficient and $\Gamma(\phi_v)$ is a function of ϕ_v - the ratio of the drift velocity, u_v , to the mean thermal velocity, $\phi_v = u_v/\sqrt{2k_BT_v/m}$. This function is a natural outcome of Schrage's selection of a drifting Maxwellian distribution for vapor molecules traveling back to the liquid surface. Comparing Eq. (1) with Eq. (2) in the limit of low evaporation rates shows that Schrage's equation predicts twice the evaporation flux as the Hertz-Knudsen equation for an AC of unity. Recent molecular dynamics simulations have shown results in line with Schrage's analysis, and ACs close to unity for a selection of fluids, including pure water at high evaporation rates.

Following Schrage's analysis, 43 Eq. (4) gives the molar evaporation flux, J^i , for the i^{th} gas component.

$$J^{i} = \sigma^{i} \sqrt{\frac{R}{2\pi M^{i}}} \left(c_{s}^{i}(T_{l}) \sqrt{T_{l}} - c_{v}^{i} \sqrt{T_{v}} \Gamma(\phi_{v}^{i}) \right)$$

$$\tag{4}$$

Here, R, is the universal gas constant, M^i , is the molar mass, $c_s^i(T_l)$ is the molar saturation concentration evaluated at the liquid temperature and c_v^i is the molar concentration at the edge of the Knudsen layer. The concentrations are related to the pressure by the ideal gas law, c = p/RT. While Eq. (3) gives $\Gamma(\phi_v^i)$, ϕ_v^i is defined for each component of the gas, as shown in Eq. (5),

$$\phi_v^i = \frac{J/c_v}{\sqrt{2RT_v/M^i}}\tag{5}$$

where the total flux and concentration for the system are $J = \sum_i J^i$ and $c_v = \sum_i c_v^i$, respectively. Eq. (5) is akin to a Mach number, denoting the ratio of the gas velocity, J/c_v , to the mean thermal velocity, $\sqrt{2RT_v/M^i}$.

For evaporation in a binary system of water and nitrogen where each component is denoted by the superscripts W and N respectively, Eq. (4) can be expanded into two mass conservation equations, Eqs. (6) and (7).

$$J^{W} = \sigma^{W} \sqrt{\frac{R}{2\pi M^{W}}} \left(c_{s}^{W}(T_{l}) \sqrt{T_{l}} - c_{v}^{W} \sqrt{T_{v}} \Gamma(\phi_{v}^{W}) \right)$$
 (6)

$$J^{N} = \sigma^{N} \sqrt{\frac{R}{2\pi M^{N}}} \left(c_{s}^{N}(T_{l}) \sqrt{T_{l}} - c_{v}^{N} \sqrt{T_{v}} \Gamma(\phi_{v}^{N}) \right)$$
 (7)

Since nitrogen is the non-condensable gas in this system, its net flux at the interface is zero, $J^N = 0$. While small amounts of dissolved gas are expected in the water droplet, it is negligible. For nitrogen at 25 °C, the mole fraction solubility is 1.183×10^{-5} , which indicates that for every mole of water evaporated, only 1.183×10^{-5} moles of nitrogen leave the droplet. Hence, J^N can be taken to be zero when compared with J^W . Furthermore, as the partial pressure of each component, p^i , must sum to the total system pressure, p, the concentrations, $c_s^N(T_l)$ and c_v^N can be written in terms of the concentrations of water vapor and the total system pressure at the interface and at the edge of the Knudsen layer, which results in the following equation.

$$\sqrt{\frac{T_v}{T_l}} = \frac{p_v - c_v^W R T_v}{p_{iv} - c_s^W (T_l) R T_l} \Gamma(\phi_v^N)$$
(8)

Here, p_{iv} is the pressure on the gas side of the liquid-vapor interface. From Eq. (8), it is clear that the temperature jump across the Knudsen layer, $\Delta T = T_l - T_v$, is linked to both the pressure difference and concentration difference across the Knudsen layer. With absolute pressure close to 10^5 Pa for systems in atmospheric conditions and the pressure ratio (p_v/p_{iv}) nearly unity, we assume a constant pressure across the Knudsen layer $(p = p_v = p_{iv})$. In this work, diffusion limited evaporation occurs at the liquid-vapor interface. However, at high evaporation flux, pressure driven flow is possible. Hence, the pressure difference between p_v and p_{iv} is cannot be neglected at high flux. Then a change in pressure over the Knudsen layer must be determined by another method so that the temperature change over the Knudsen layer can be computed as in Eq. (8).

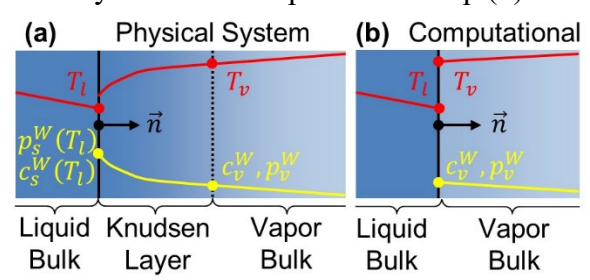


Figure 1. (a) Physical system described by the kinetic theory of gases with the Knudsen layer. (b) An equivalent computational model that neglects the Knudsen layer but accounts for temperature and concentration discontinuities.

Providing an accurate value for $J = J^W$ using Eq. (6) is the main challenge for modeling evaporation. Since the Knudsen layer thickness is comparable to the mean free path, computational models for continuum analysis often neglect the variation of properties across the Knudsen layer (Figure 1(a)). We use the kinetic theory of gases to account for the temperature and concentration variations in the Knudsen layer, which can be incorporated in the computational models as vapor concentration and temperature jump conditions, as illustrated in Figure 1(b). In this regard, the temperature across the Knudsen layer will vary from T_l to T_v , as determined by Eq. (8). While Eq. (8) can be solved analytically, the solution for T_v is unwieldy. Here, we propose a simplification (see supplementary material) to calculate T_v as an explicit function of T_l .

$$T_{v} \approx T_{l} + \frac{2R}{p} (c_{s}^{W} - c_{v}^{W}) T_{l}^{2} + \frac{R^{2}}{p^{2}} (c_{s}^{W} - c_{v}^{W}) (3c_{s}^{W} - 5c_{v}^{W}) T_{l}^{3}$$

$$\tag{9}$$

Equation (9) allows determining the temperature jump using parameters at the liquid-vapor interface (T_l) , and the edge of the Knudsen layer (p, c_v^W) , which are related to the variables solved by the continuum models, making it possible to analyze evaporation under different operating conditions using standard software packages.

2 Methods

2.1 Experimental Technique

Precise experimental techniques are needed to investigate evaporation and quantify the AC. In this study, we monitor the geometry of an evaporating droplet with high accuracy to quantify the evaporation rate. In this regard, we use a quartz crystal microbalance (QCM) as an accurate sensor to determine the droplet radius and the amount of non-volatile impurity in the evaporating water. QCM devices are typically used as film thickness monitors in deposition processes with sensitivities close to ng/cm² (see supplementary material). This high sensitivity to surface phenomena makes it a tool of interest for studying the evaporation of droplets and other wetting and surface phenomena. While the QCM can be misunderstood to operate like a typical microbalance, QCMs may not respond to mass changes directly but to the acoustic properties of the adjacent media. For example, the shear stress exerted by a Newtonian fluid drop on the oscillating surface of the QCM affects its response. Recently, Murray *et al.* showed how QCMs, as a radius sensor, reduce the overall uncertainty in measuring droplet volume during evaporation by a factor of six compared to high-resolution visual images alone. We use this approach in this work as well.

Equation (10) relates the QCM's frequency shift to the droplet contact radius, r_a , where the QCM electrode radius is denoted as r_e (Figure 2(a)). Here, a is an intrinsic constant that can vary depending on the type of QCM used. In this case, a = 1 since this study uses a planar AT-cut crystal with concentric keyhole-shaped electrodes (Figure 2(a)). ^{73,96–98,74}

$$\Delta f = -f_0^{\frac{3}{2}} \sqrt{\frac{\rho \mu}{\pi \rho_q \mu_q}} \left(1 - e^{-2a\frac{r_d^2}{r_e^2}}\right)$$
(a)
$$r_e$$
Electrode
$$r_q$$
Quartz Crystal

(b)
Camera
Chamber
Humidity
Sensor
QCM Electrical
Connection
Thermocouple
Windows

Figure 2. (a) The top and cross-sectional views of the QCM loaded with a centrally placed sessile droplet. The QCM used in this work is a planar AT-cut crystal with concentric keyhole-shaped electrodes. (b) Overhead schematic of the experimental chamber and a QCM loaded with a backlit droplet imaged using a camera, with additional sensors and the nitrogen inlet. Not shown is the flow outlet directly above the droplet, which also allows a syringe needle to enter the enclosure from the top to deposit the water droplet on the QCM.

Note that Eq. (10) does not indicate contact angle dependence. Our previous work has found that contact angle only influences the frequency response for microscopically-thin droplets.⁷³ For example, the frequency response of a 10 MHz QCM loaded with a 1 mm diameter water droplet is only affected by changes in the contact angle when the contact angle is less than 0.02° . Thus, the frequency response is mainly related to the droplet radius, where the sensitivity of the QCM to radial changes is 1 Hz/ μ m. Therefore, a QCM can be used as a high-precision contact radius sensor to quantify droplet evaporation. Meanwhile, we use droplet imaging to measure the change in contact angle during evaporation, as illustrated in Figure 2(b).

Noting that impurities can affect the AC, we use the same setup to quantify the impurity content (~nanograms) in the droplet. This aspect is often overlooked with the assumption that the evaporating water is pristine, which in many cases is not accurate. However, eliminating all impurities is a daunting challenge since even the most pristine sources of water and clean setups can consist of microscopic contaminants. During evaporation, the QCM frequency increases continuously to approach the unloaded resonant frequency. However, the experiments typically result in a slight difference between the initial and final resonant frequencies due to non-volatile impurities in the droplet. To determine the non-volatile impurity content, Δm , in the droplet, we use Eq. (11). The mean frequency, after it stabilizes within 1 Hz, determines the net frequency shift. The frequencies, recorded at 5 samples/second, stabilized in the final 30-60 seconds for all the trials. In order to use Eq. (11), the inner radius of impurity deposition must be known and can vary as $0 \le r_i < r_o$ giving a low estimate at $r_i = 0$ and high estimate at $r_i = r_o$. The supplementary material provides more details on impurity quantification.

$$\Delta f = -C_f \frac{\Delta m}{\pi (r_o^2 - r_i^2)} \left(e^{-2a\frac{r_i^2}{r_e^2}} - e^{-2a\frac{r_o^2}{r_e^2}} \right)$$
(11)

The calculation of evaporation rate and AC relies on the accuracy of radial and volumetric measurements during evaporation. A combination of droplet visualization and QCM frequency measurements achieves this objective. A goniometer (Ramé-Hart 590-U2) provides image-based measurements to determine the droplet's contact angle

over time. The goniometer images a backlit droplet and determines the liquid-vapor interface to find the droplet's contact angle.

Meanwhile, the frequency response of the QCM determines the droplet radius over time. For each experiment, the unloaded frequency of the QCM, f_0 is defined as the mean frequency recorded before depositing the droplet. The QCM is periodically calibrated by submerging it in deionized water to obtain a frequency shift relative to its operation in the air. This frequency shift corresponds to Δf_K and the leading terms in Eq. (10). With these values, the radius of the droplet, r_d , can be determined using Eq. (10).

The height, h, of the sessile droplet is calculated as shown below (Eq. (12)), assuming a spherical cap, where θ is the contact angle obtained from the goniometer. The volume, V, of the sessile droplet is calculated as Eq. (13). Both Eq. (12) and Eq. (13) are geometrical relationships of a spherical cap. The droplet radius is less than the capillary length for water. The droplets are also large enough to neglect the extension due to disjoining forces. Hence, the spherical cap assumption used in this study is reasonable. The supplementary material contains additional details supporting this assumption.

$$h = r_d \tan \frac{\theta}{2} \tag{12}$$

$$V = \frac{\pi h}{6} (3r_d^2 + h^2) \tag{13}$$

The time derivative of the volume (dV/dt) gives the volumetric evaporation rate (\dot{V}) . The average evaporation flux, \bar{J}^w can be calculated as the ratio of the volumetric rate and droplet surface area, \dot{V}/A , where $A = \pi (r_d^2 + h^2)$. A piecewise linear fit was applied to the raw volume data to minimize the noise in the calculated volume derivative and determine the evaporation rate.

Uncertainty analysis is carried out on each experimental parameter, which is then used in conjunction with sensitivity analysis of the computational model to determine the uncertainty in the resulting AC. Further details can be found in the supplementary material.

2.2 Experimental Procedure

All experiments involved a cleaning procedure for the QCM to ensure a clean crystal surface. The cleaning procedure consisted of a series of sonication steps in various solutions, including 50 mM NaOH, 1 part Toluene to 2 parts Acetone, Acetone, Isopropyl Alcohol, and finally DI water. The QCM was suspended in each of these solutions for at least 5 minutes. In between sonications, the QCM was washed via a syringe with the next solution. After finishing the DI water sonication, the QCM was dried using a pure nitrogen gas stream, then placed into the sealed chamber until measurements began.

Experiments to evaluate the AC of sessile droplets were conducted inside an enclosure (Figure 2(b)) maintained at room temperature. The temperatures recorded with ± 0.5 °C uncertainty indicated a constant temperature in the enclosure during experiments. Nitrogen gas was supplied to the enclosure at low speed, with the flow rate recorded using a rotameter (± 5 L/hr uncertainty). The nitrogen flow allowed displacing moisture in the enclosure to maintain a constant humidity of 0%–2%. Ultrahigh purity nitrogen gas (99.999% N₂, Airgas) was chosen as the process gas for its consistency in properties and similarity to dry air that is typically used in industrial applications. Humidity and temperature measurements were acquired using Honeywell HIH-4000 and J-Type thermocouples, respectively. The humidity sensor and a thermocouple were placed in the upstream flow to capture the inlet conditions, and a second thermocouple was placed in the downstream flow. Contact angle measurements took place using transparent enclosure windows, as illustrated in Figure 2(b). Experiments used deionized (DI) water with evaporation residue < 1 ppm (HiPerSolv, VWR). Droplets approximately 2-4 μ l in volume were deposited onto the QCM via a manual glass syringe equipped with a clean 22-gauge stainless steel needle entering the enclosure through a 1/8 in. diameter hole directly above the center of the QCM. The droplets were initially at ambient temperature and pressure. This 1/8 in. diameter hole also served as an outlet for vapor flow. The

frequency response of the planar 10 MHz AT-cut polished QCM with keyhole-shaped gold electrodes (Figure 2(a)) was recorded using an eQCM system (Gamry Instruments). The gold-coated surface was chosen for inertness and reusability to get consistent wetting dynamics.

The QCM measurements include recording frequency several minutes before droplet deposition to form a reliable baseline frequency. The droplet was then deposited onto the center of the QCM. Frequency, humidity, and temperature measurements were recorded throughout the deposition and evaporation process. After droplet deposition, the droplet was brought into focus using the goniometer to continuously record the contact angle for the duration of the experiment. Data acquisition was completed approximately 60 seconds after the droplet had evaporated completely and the frequency response of the QCM plateaued. All measurements were then stopped, and the QCM remained in the sealed chamber until the next experiment.

2.3 Computational Modeling

The computational model supplements the experiments to quantify the AC. Assuming quasi-steady evaporation, the computational model determines the temperature, pressure, and vapor concentration in the ambient for a droplet undergoing evaporation in a dry environment. The quasi-steady assumption in this model involves a static droplet geometry and solving for a stationary solution. The applicability of this assumption is included in the supplementary material. As mentioned earlier, the model does not explicitly solve the Knudsen layer but considers jumps in properties (temperature, vapor concentration) based on the kinetic theory of gases. Thus, it combines evaporation, conduction, convection, and radiation mechanisms in the water and surrounding gas domains using the finite element method framework provided by COMSOL Multiphysics software. More details regarding the model, including a schematic of the computational model, boundary conditions, material properties, and uncertainty analysis, are contained in the supplementary material.

Fourier's law (Eq. (14) and conservation of energy (Eq. (15)) govern heat transfer in the solid, liquid, and vapor domains. In the liquid domain, since the characteristic temperature and velocity gradients are relatively small, convection and radiation are negligible compared to heat conduction. Although thermocapillary effects can cause flow inside droplets, these effects are negligible for tiny water droplets and small evaporation rates. Therefore, the velocity in the liquid domain was taken as $\mathbf{u} \approx 0$. In the vapor domain, heat transfer by convection is considerable and is governed by Eqs. (14) and (15) with a nonzero \mathbf{u} .

$$q = -k\nabla T \tag{14}$$

$$\rho C_p \boldsymbol{u} \cdot \nabla T + \nabla \boldsymbol{q} = 0 \tag{15}$$

In Eqs. (14) and (15), q is the heat flux vector, k is the thermal conductivity, T is temperature, ρ is the fluid density, C_p is specific heat capacity, and u is the velocity in the vapor domain. In the vapor domain, the flow field is affected by the nitrogen stream, water vapor concentration, and temperature gradients, causing density variations and making buoyancy effects significant. The governing equations of flow in the vapor domain are

$$\rho_{v}(\boldsymbol{u}\cdot\nabla)\boldsymbol{u} = \nabla\cdot\left[-p\boldsymbol{I} + \mu_{v}(\nabla\boldsymbol{u} + (\nabla\boldsymbol{u})^{t})\right] - \rho_{v}g\hat{z}$$
(16)

$$\nabla \cdot (\rho_v \mathbf{u}) = 0 \tag{17}$$

where ρ_v and μ_v are the density and dynamic viscosity of the water-nitrogen gas mixture, respectively, g is the acceleration due to gravity in the negative \hat{z} direction, I is the identity matrix, and superscript t denotes transpose. Diffusion and convection govern water vapor transport in the ambient nitrogen gas, as shown in Eq. (18).

$$\nabla \cdot (-D\nabla c^W + \boldsymbol{u}c^W) = 0 \tag{18}$$

Here D is the diffusivity and c^W is the concentration of water vapor in nitrogen. We should note that the governing Eqs. (14) to (18) are standard and solvable using various software packages. However, in evaporation, a crucial model input is the interface conditions provided as follows.

The evaporation flux in the model, which is a boundary condition provided from experimental observations, is enforced by an integral constraint on the droplet's surface, as shown in Eq. (19). The measured volume rate of change in the experiment, \dot{V} , controls the molar evaporative flux on the droplet, $n \cdot J$, where J depends on the gradient of vapor concentration at the liquid-vapor interface (Eq. (20)).

$$-\dot{V} = M^W \iint \frac{1}{\rho_l} \boldsymbol{n} \cdot \boldsymbol{J} \, dA \tag{19}$$

$$\mathbf{J} = -D\nabla c^W \tag{20}$$

Here ρ_l is the mass density of liquid water at the interface. Note that J determined using Eq. (20) can also be equated to the vapor flux derived from kinetic theory (Eq. (6)), which allows determining the local and average mass accommodation coefficient, σ^w .

3 Results and Discussion

The AC can be calculated if the evaporation flux, liquid and vapor temperature, and water vapor concentration at the edge of the Knudsen layer are known (Eq. (6)). The following sections describe the evaporation kinetics observed in multiple experiments using the QCM. Using the evaporation rates from experiments in the computational model, we determine the average AC for water evaporating into dry nitrogen. Since the calculation of local AC depends on several parameters, we discuss briefly how local temperature, concentration, and flux vary across the surface of an evaporating water droplet. Finally, we also show how our simplified interfacial flux model and the accurate value of AC can yield good agreement with evaporation experiments in other settings.

3.1 Droplet Evaporation Experiments

We performed multiple experimental trials involving evaporation of sessile water droplets (2-4 μ L) at room temperature (23.5-25.5 °C). Figure 3 shows the variation of different parameters in multiple trials consisting of different initial droplet volumes.

The first row of Figure 3 shows the QCM's frequency response of the evaporating droplets. The frequency response shows two distinct modes corresponding to the constant contact radius (CCR) and the variable contact radius (VCR) modes of evaporation. These modes were also noted by Picknett and Bexon²⁹ in their landmark study. The transition from the CCR to the VCR mode occurs where the frequency response changes from nearly constant to an increasing value. Physically, this change represents the droplet de-pinning itself on the QCM surface. During evaporation, the contact angle decreases until the receding angle is reached, at which point the CCR mode ends, and the VCR mode begins. At this point, the contact line de-pins, and the frequency begins to increase, as expected from Eq. (10). The frequency continues to increase to a value just less than the unloaded resonant frequency. The slight difference between the initial (unloaded) and final resonant frequencies corresponds to the mass of non-volatile impurities from the water droplet. The non-volatile impurities in each droplet are on the order of nanograms that are not macroscopically visible. Hence, in typical evaporation experiments, these values are seldom reported. However, it is crucial to know the impurity content in the evaporating water to understand its effect on the accommodation coefficient.

The frequency shift of the QCM after complete evaporation determines the impurity mass based on Eq. (11). The amount of non-volatile impurities is tabulated in Table 1, which shows that the high and low estimates vary by approximately 30%. The highest amount of mass, 100 ng, is minimal to be captured by conventional microbalances. While state-of-the-art mass balances have resolutions close to 100 ng, the corresponding -120 Hz frequency shift for the QCM is significantly larger than its 1 Hz resolution. The parts per million (ppm) measurements of the impurities are calculated in terms of mass fractions using the droplet's initial mass. The water used in these experiments has an evaporation residue of 1 ppm by weight. So, it can be inferred that some

contaminants came from the laboratory environment. In non-QCM based sessile droplet evaporation, it would be nearly impossible to quantify impurities to this precision and of this magnitude.

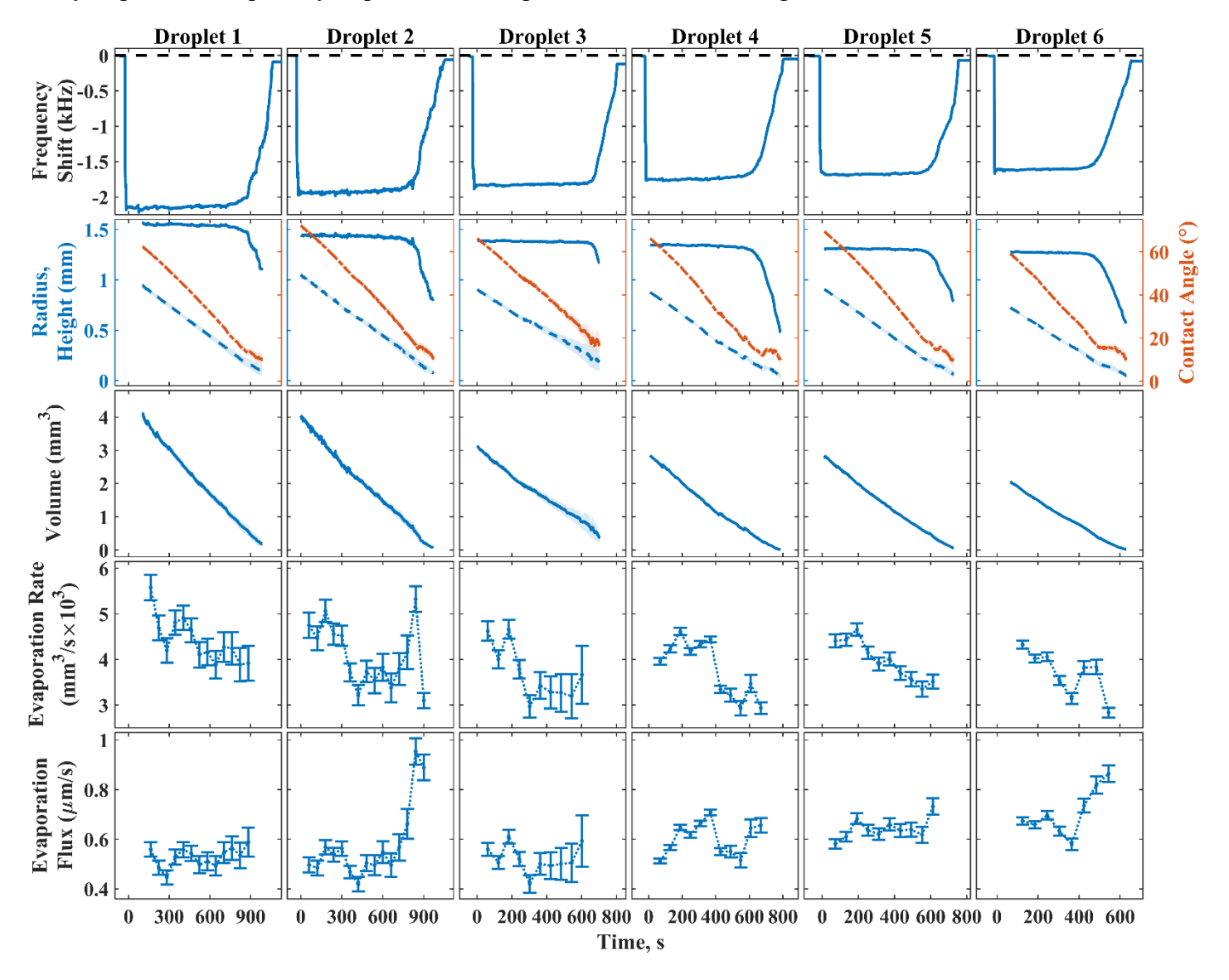


Figure 3. Six experimental trials of droplet evaporation are shown in separate columns with their measured quantities in rows: frequency shift (first row), radius (second row, solid line), height (second row, dashed line), contact angle (second row, dash-dotted line), volume (third row), evaporation rate (fourth row), and evaporation flux (fifth row).

Table 1: Measured non-volatile impurities in evaporated droplets

Droplet:	1	2	3	4	5	6
Final Δf (Hz)	-88.6	-60.0	-120.8	-50.8	-67.8	-78.5
Low Estimate (ng)	58.0	37.6	73.8	30.6	40.3	46.0
High Estimate (ng)	85.8	52.9	100.3	40.8	52.9	59.4
Low Estimate (ppm)	14.2	9.3	23.5	10.8	14.4	22.6
High Estimate (ppm)	21.0	13.1	32.0	14.4	19.0	29.2

The second row of Figure 3 shows the change in radius and contact angle during droplet evaporation. Each trial's radius measurement is flat until the receding contact angle is reached. Although the contact angle shows a general decreasing trend in most experiments, minor differences among the trials result from variations in the surface energy caused by slight differences in cleaning, handling, and environmental factors. Consequently, we also see a little spread in the receding angle of $17^{\circ} \pm 2^{\circ}$. The droplet's height decreases almost linearly and does not have any abrupt change during the transition from the CCR to VCR mode. Error bands are included in the radius, contact angle, and height measurements. The accuracy of the radius measurement using the QCM is high, with the uncertainty smaller than the line width. In the case of the contact angle, the uncertainty is small when the droplet is large but increases as the contact angle decreases.

The evaporation rate of each droplet is shown in the fourth row of Figure 3. The error in the calculation of the evaporation rates was obtained by York's method. ^{74,101} This method determines the slope and the intercept for a line fitting the volume versus time curve, which yields the evaporation rate every 60 s. More details regarding this method are provided in the supplementary material. The initial droplet evaporation rate depends on the droplet size, specifically on the radius. The evaporation rate generally decreases over time in all the trials. Compared to the average evaporation rate, larger droplets (Droplet 1) have slightly higher evaporation rates, while smaller droplets (Droplet 6) have marginally lower evaporation rates for similar ambient conditions. Due to the comparable initial size of the droplets, this observation is small but discernable in the fourth row of Figure 3. This size dependence agrees with diffusive theories of sessile droplet evaporation, where the evaporation rate is proportional to the droplet contact radius. ³⁰ The last few data points in row 4 of Figure 3 in all trials are not as accurate as the initial data points. This observation is mainly due to two factors: (1) the volume data is more accurate when the contact angle is large, and (2) the droplet may not be receding evenly, which would violate the assumptions of Eq. (10). This trend can be seen quantitatively in the relative size of the error bars, wherein the error bars grow proportional to the uncertainty in volume measurement towards the end of evaporation.

Non-monotonicity in each droplet's evaporation rates can be attributed to many competing factors, most importantly, the temperature variations during evaporation and vapor recirculation in the test chamber. The recirculation in the chamber would cause the overall moisture content in the test chamber to vary with time, influencing the droplet's evaporation rate. A thermocouple 5 inches (12.7 cm) upstream from the droplet indicated a 0.1-0.6 K decrease in the chamber temperature due to evaporative cooling of incoming air. Considering the thermocouple uncertainty (±0.5 K), a slight decrease in upstream chamber temperature indicates some flow recirculation inside the chamber. Our previous work on the evaporation of sessile droplets also showed that the QCM temperature decreases due to self-cooling, which is expected here as well.⁷⁴ In this study, the self-cooling of the droplet and the experimental chamber is captured in more detail via the computational model discussed later.

The fifth row of Figure 3 shows the evaporation flux in each droplet. For most of the droplet lifetime, the evaporative flux is constant within measurement uncertainty. Notably, the time-averaged evaporation flux is lowest for the largest droplet (Droplet 1), with the smallest droplet (Droplet 6) having the highest flux throughout evaporation. This inverse relationship between droplet size and evaporative flux can be best explained by lower droplet self-cooling, which increases the average saturation concentration at the droplet surface, corresponding to a higher average evaporation flux. The temperature dependence of water vapor saturation pressure far outweighs the effect of curvature as described by Kelvin's equation. Using a radius of curvature of 1 mm would lead to vapor pressure increasing only by a factor of 1.000001, whereas a 1 °C increase from 20 °C to 21 °C would increase the vapor pressure by about 150 Pa - a factor of 1.06.

3.2 Droplet Temperature

The QCM is a thermally insulating surface under the evaporating droplet, which allows for self-cooling that affects evaporation kinetics. The heat capacity of the QCM crystal is also low due to the small size (7 mm radius, 0.16 mm thickness) and moderate specific heat (740 J/kgK) of quartz. Moreover, heat transfer from the ambient

atmosphere to the QCM is limited due to the low-speed flow. In effect, these factors result in comparable QCM and droplet temperatures. The computational model discerns these effects of self-cooling due to evaporation.

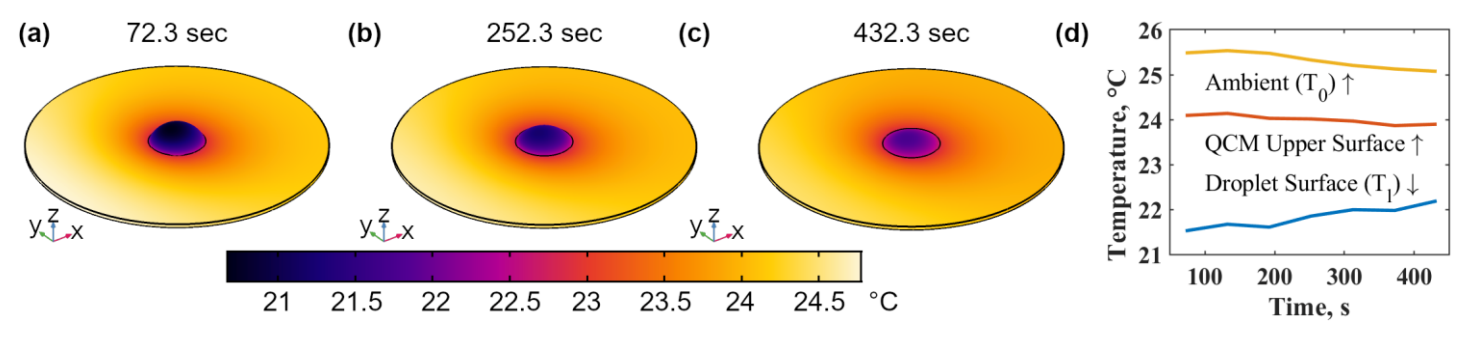


Figure 4: (a)-(c) Temperature contour plots on the surface of the QCM and droplet (T_l) of Droplet 5 at times 72.3, 252.3, and 432.3 seconds, respectively. (d) Surface averaged temperature (T_l) , QCM upper surface temperature, and ambient temperature (T_0) over time of Droplet 5. Nitrogen flow is in the positive x-direction.

Figure 4(a)-(c) show the model-predicted temperature of the droplet and QCM surface (for Droplet 5) at various times. The effect of the nitrogen flow is noticeable, however, minor. In a purely diffusive environment, the temperature profile across the droplet and QCM surface would be symmetric. However, nitrogen flowing in the x-direction causes a non-symmetric temperature variation, with a minimum upstream. This asymmetry is due to higher self-cooling upstream via increased vapor advection even though the nitrogen gas is warmer than the droplet. The flow pattern around the droplet and the vapor flux distribution on the droplet can be seen in Figures S2 and S3 in the supplementary material, respectively. Over time, the droplet's average temperature increases due to (a) the decreasing size, which makes heat diffusion across the droplet more efficient, and (b) the decreasing evaporation rate, which slows self-cooling. Consequently, the droplet surface and QCM temperatures start to converge, as shown in Figure 4(d).

3.3 Vapor Concentration at the Edge of the Knudsen Layer

Figure 5(a)-(c) show the water vapor concentration on the droplet's surface over time (for Droplet 5). The vapor concentration is the highest near the base of the droplet, where the temperature is highest. As the droplet evaporates and becomes more isothermal, the difference between concentration at the apex and base decreases. Due to the relationship between temperature and concentration (Eq. (8)), the minimum concentration is also on the droplet's upstream side, where the temperature is minimum. The minimum concentration increases over time as the droplet becomes warmer compared to the initial conditions.

Figure 5(d)-(f) show water vapor concentration and temperature on the yz-plane - the mid-plane through the droplet normal to flow direction. The vapor concentration contours show wider spacing near the droplet's apex than the contact line, implying a larger flux from the droplet at the base than the apex. This phenomenon is particularly acute in Figure 5(f), where the droplet has a low contact angle. The concentration drops sharply away from the interface due to dry nitrogen gas flow around the droplet.

The temperature cross-sections in Figure 5(d)-(f) illustrates the effect of self-cooling on the droplet and the QCM. The droplet's self-cooling lowers the QCM's temperature, resulting in a sizeable temperature gradient across the crystal in the radial direction. The surrounding nitrogen gas, which is at ambient temperature, heats the QCM to balance the self-cooling. Figure 5(d)-(f) also show the temperature discontinuity across the liquid-vapor interface where the vapor temperature is greater than the liquid temperature. To balance self-cooling, heat conduction from the base and the top (across the Knudsen layer towards the liquid-vapor interface) requires the liquid temperature at the interface (T_l) to be lower than both the base and the vapor temperature (T_v). This observation is in line with previous efforts on unheated water evaporating into atmospheric conditions that have also shown $T_l < T_v$.²⁶

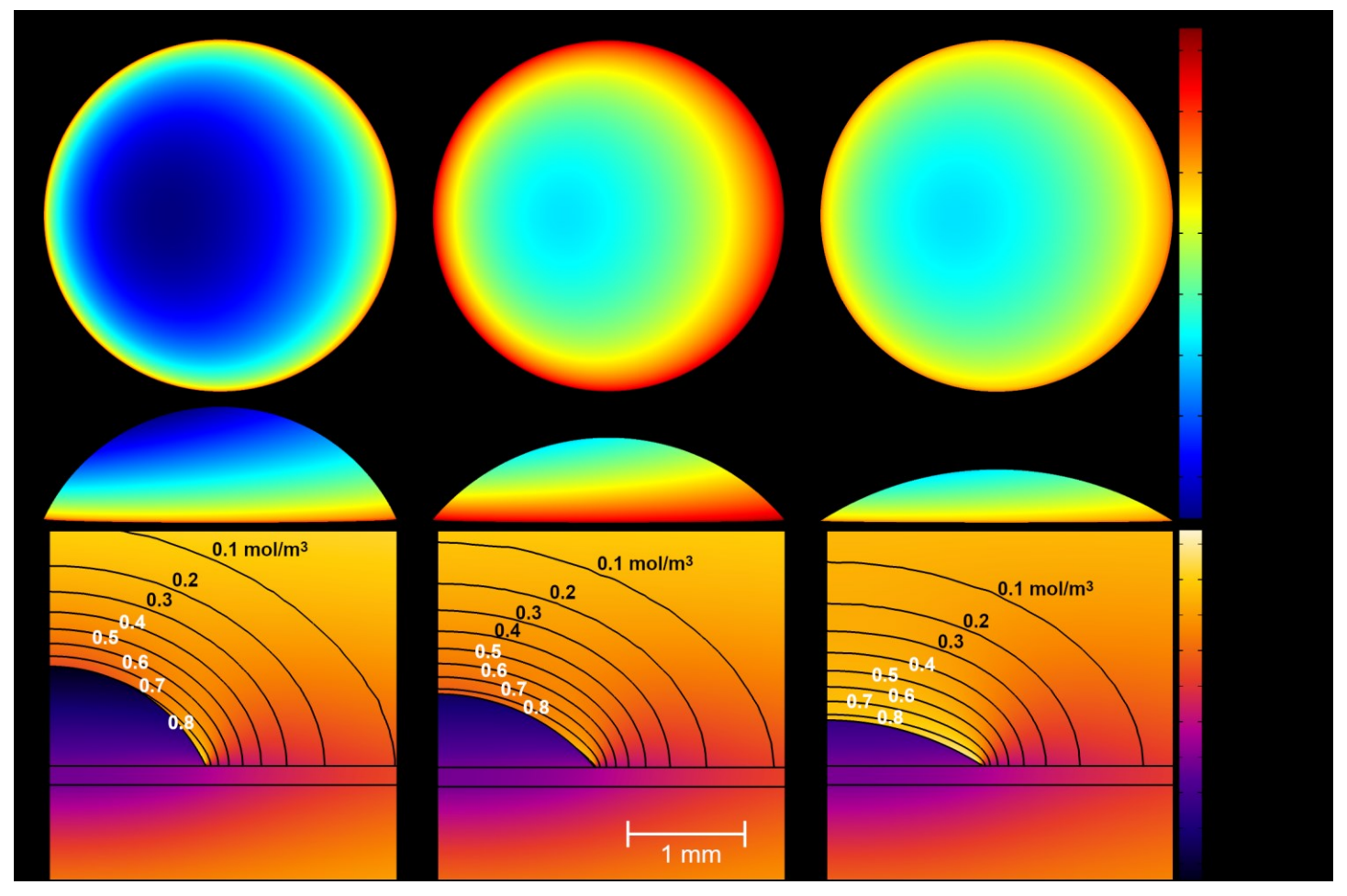


Figure 5. (a)-(c) Water vapor concentration (mol/m³) on droplet surface (top and side views) at times 72.3, 252.3, and 432.3 seconds, respectively. (d)-(f) Contour plot (labeled black lines) of water vapor concentration (mol/m³) and the shaded (colored) plot of temperature (°C) on the yz-plane cross-section at time 72.3, 252.3, 432.3 seconds, respectively.

3.4 Flow Pattern

The inlet nitrogen stream is level with the QCM, and the QCM acts like a flat plate where a boundary layer forms, as shown in Figure 6. The incoming flow has a low stagnation point on the front of the droplet, while flow separation occurs behind the droplet, where a small flow recirculation occurs on the far downstream side of the droplet. These streamlines, highlighted in red, are also shown in the insets of Figure 6(a) and (b). These streamlines later form a vortex at the trailing edge of the QCM surface. As the droplet evaporates, the contact angle decreases, with the front stagnation point disappearing and the recirculation area decreasing, as shown in Figure 6(b) and (c), eventually leading to an attached flow, as shown in Figure 6(c). The inset to Figure 6(b) shows how the recirculating streamlines occur over less area, and the black streamlines stay attached to the droplet surface for longer distances relative to streamlines in Figure 6(a). Later in the experiment, the streamlines are fully attached across the QCM surface, as shown in Figure 6(c), and these few streamlines form a much smaller vortex relative to Figure 6(a).

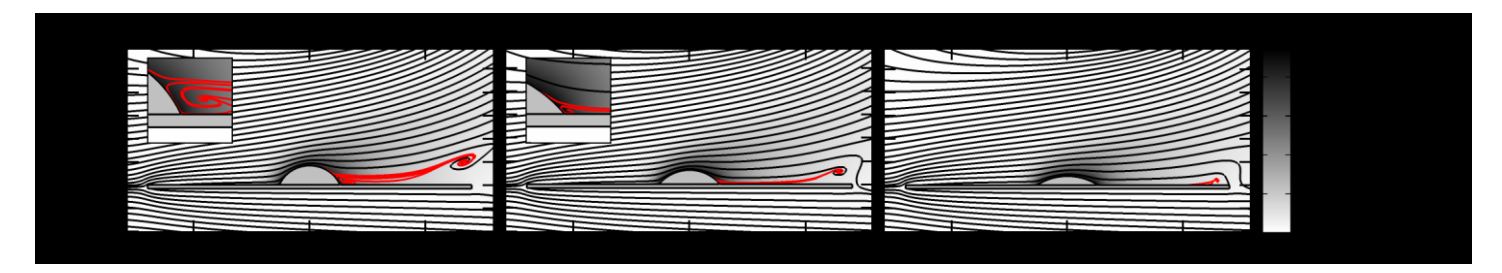


Figure 6. Velocity streamlines and concentration distribution on xz-plane (symmetry plane) of Droplet 5 at times 72.3, 252.3, and 432.3 seconds, respectively. Insets to (a) and (b) show streamlines on the droplet's downstream side near the QCM surface. Streamlines, highlighted in red, show stagnation points or vortices.

Figure 6 also shows the concentration profile in the QCM and droplet along the symmetry plane. The concentration profile downstream is higher than that upstream of the droplet due to the advection from the nitrogen flow carrying vapor across the droplet's surface. With decreasing droplet contact angle, vapor advection increases, with a notable difference behind the droplet.

The changes in flow patterns during evaporation can have interesting effects. In a purely diffusive isothermal environment, the evaporation rate would be expected to decrease as the contact radius and contact angle decrease $(\dot{V} \propto r_d, \theta^2)$. However, the evaporation rate may not monotonically decrease with time in an advective-diffusive environment. While the flow pattern changes, the droplet's temperature rises, and the droplet geometry changes (contact radius, contact angle decreasing), each having competing effects on the evaporation rate. The overall balance of these effects determines the evaporation rate and can make for a non-monotonic change in rate over time, as seen in the evaporation rate measurements in the fourth row of Figure 3.

3.5 Evaporation Flux Distribution

While the experiments determine the total evaporation rate and average flux, the computational model indicates how local evaporation flux varies across the droplet surface. Figure 7 shows the evaporation flux along three lines on the droplet surface, directly facing the nitrogen flow $(0^{\circ}, y = 0, x \le 0)$, perpendicular to the flow direction $(90^{\circ}, y \ge 0, x = 0)$ and along the flow direction $(180^{\circ}, y = 0, x \ge 0)$ for Droplet 5 at various times. The inset in each Figure 7(a)-(c) shows the orientation of the lines on the droplet. The flux on the droplet's surface is the lowest at the apex and has a singularity at the contact line, which is also found in simple diffusive theories.³⁰

Differences are observable between fluxes along the different lines on the droplet. The flux on the droplet's upstream side (along 0°) is the highest as anticipated, while the flux on the downstream side (along 180°) is the lowest. Values along both lines converge at the apex, as they all share the same point. The cause of the reduced evaporation flux on the downstream side is due to higher vapor concentration and lower concentration gradients. The minimum flux on the droplet occurs along the 180° line, approximately halfway up the droplet. The flux along the line perpendicular to flow (along 90°) lies between the fluxes along 0° and 180°. This variation indicates a near monotonic decrease in flux from the droplet upstream to the downstream side along the azimuths.

As the droplet evaporates, the flux does not change significantly in value, which is expected as the average flux (Figure 3, fifth row for Droplet 5) is nearly constant over time. However, at the contact line, the local evaporative flux increases as the droplet contact angle decreases with time, which is in line with analytical solutions to diffusion flux from spherical droplets. ^{29–31,33,34} The computational model indicates that the evaporation flux at the contact line varies more gradually in the initial stages but changes more sharply at later stages as the droplet becomes small and the vapor gradient increases, as shown in Figure 5(f).

Figure 7 (right vertical axis) shows the ratio of the local molar flux to the local AC (J/σ) . This ratio is equivalent to the driving potential term, $(c_s^W(T_l)\sqrt{T_l}-c_v^W\sqrt{T_v}\Gamma(\phi_v^W))$, of Eq. (6). Here, the value of this ratio is nearly constant over the majority of the droplet surface but changes slowly in time, which implies that the term

 $(c_s^W(T_l)\sqrt{T_l} - c_v^W\sqrt{T_v}\Gamma(\phi_v^W))$ of Eq. (6) varies slowly over the droplet, and most of the variation in the local AC is only near the contact line. The values of T_l , T_v , and c_v^W are determined directly from the computational model.

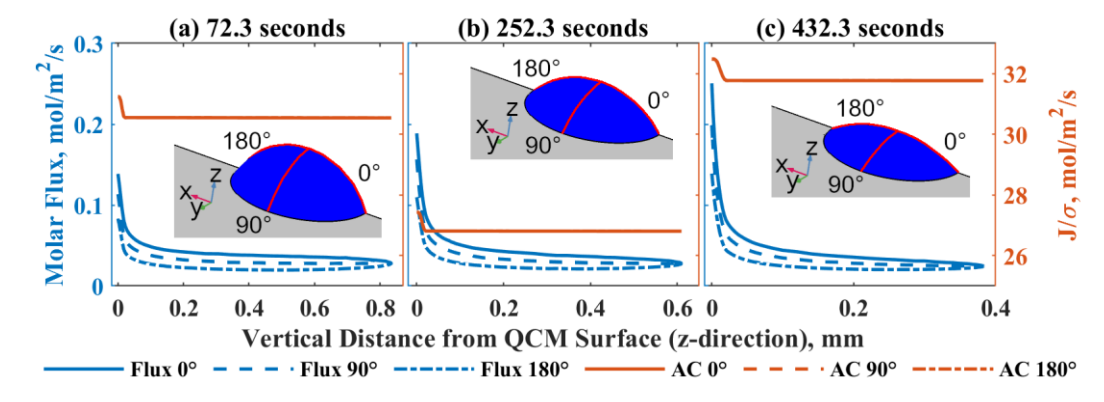


Figure 7. Flux distribution and the ratio of flux to accommodation coefficient (J/σ) on droplet surface facing the nitrogen flow $(0^{\circ}, y = 0, x \le 0)$, perpendicular to the flow direction $(90^{\circ}, y \ge 0, x = 0)$ and opposite the flow direction $(180^{\circ}, y = 0, x \ge 0)$ for Droplet 5 at times 72.3, 252.3, and 432.3 seconds, respectively. The lines denoting the ratio of flux to accommodation coefficient are shown directly on top of one another.

3.6 Accommodation Coefficient of Water Evaporating in Dry Nitrogen

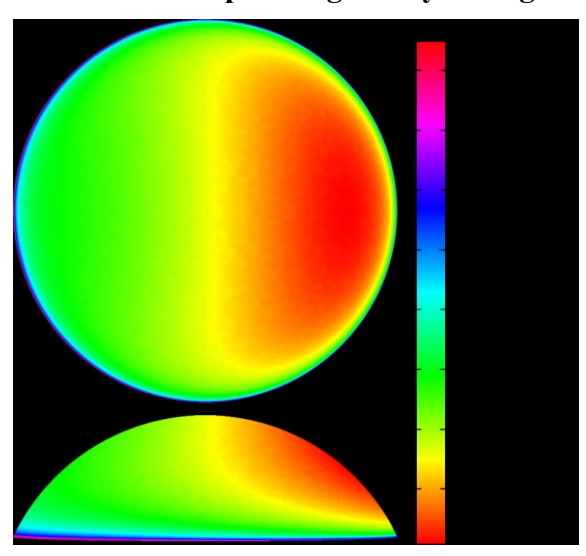


Figure 8. Distribution of AC on the surface of the evaporating droplet in Droplet 5 at 72.3 seconds. Similar distributions are also seen at later times.

Figure 8 shows a snapshot of how the accommodation coefficient (Eq. (6)) varies over the droplet's surface for Droplet 5 at 72.3 seconds, varying almost by a factor of 5 from minimum to maximum. As mentioned before, the calculated values of AC depend on several factors, including the evaporation flux observed in the experiments, the predicted variation of temperature and concentration. The AC is highest at the droplet's contact line and is the lowest on the downstream side, just below the apex. This lowest AC region is also where the temperature is relatively high that corresponds to a higher saturation vapor concentration and minimum flux due to flow recirculation affecting vapor concentration and transport. The maximum calculated value of AC occurs along the contact line, where evaporation flux is maximum.

3.7 Accommodation Coefficient

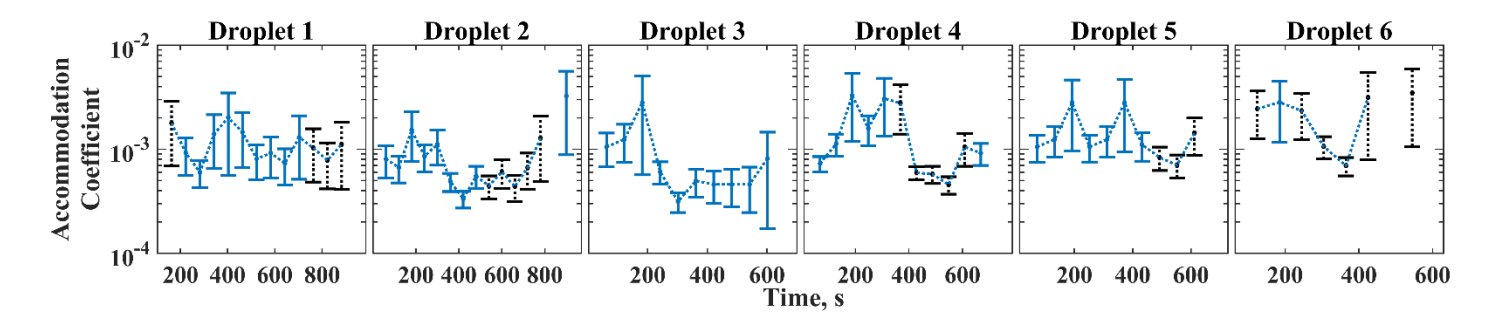


Figure 9. The surface-averaged accommodation coefficient over time for each experimental trial. Note that these values correspond to droplet evaporation close to room temperature. Blue points and solid error bars are from the quasi-stationary solution of the computational model. The black points and dashed error bars are from a modified model (see supplementary material).

Over the lifetime of the droplet, the AC can change due to multiple factors, including interfacial conditions such as temperature, accumulation of non-volatile impurities, and changes in ambient vapor concentration. Figure 9 shows how the average AC changes over time for each droplet. Overall, the accommodation coefficient is nearly constant during evaporation in every trial, even as the evaporation rate decreases, temperature increases, and unavoidable non-volatile impurities accumulate. The average AC lies around 0.001 under these conditions across the six trials. The value of $\sigma = 0.001$ is determined from a weighted average of the data in Figure 9. This information is tabulated in the supplementary material. Droplet 3, however, shows a trend of decreasing AC with time, which could be due to the accumulation of impurities in the droplet. This droplet contained the highest amount of deposited solids (Table 1) measured in ppm of all experimental trials, making any effect of impurities most visible in this trial. Experiment-averaged values of AC close to 0.001 have been reported before in some experiments. However, in this study, the AC is not averaged over the lifetime of the droplets and is determined as a function of time while the droplet undergoes a dynamic process. Additionally, the accumulation of non-volatile impurities (Table 1) and a high non-condensable gas mole fraction of 0.97 at the liquid-vapor interface are factors affecting the AC value, which are quantified in this study.

Furthermore, it is essential to quantify uncertainty in the reported values of AC. The error bars shown in Figure 9 are determined by numerically finding the sensitivity of the average AC to the three main input parameters to the computational model, the evaporation rate, the ambient chamber temperature, and the nitrogen flow rate. We did not include AC for Droplet 2 at 840 seconds and Droplet 6 at 485 seconds due to the uncertainty associated with these points, which were orders of magnitude higher than the remaining points. Details included in the supplementary material show the contribution from each parameter to the total error (Figure S3).

3.8 Application of the Evaporation Flux Model and AC

Additional experiments of sessile droplets evaporation were performed to gauge the accuracy of the evaporation flux model, and the AC of 0.001 observed under similar operating conditions. In this case, sessile drops of approximately 3 µL were deposited on a 12x12x2 mm aluminum nitride heater (Watlow) inside the same experimental enclosure (Figure 2(b)) with nitrogen cross-flow. The goniometer was used to monitor droplet volume. Constant heat flux was supplied to the heater in the four experiments, with the heater temperature measured by an integrated K-type thermocouple. Table 2 gives an overview of the experiment parameters. The volumetric flux of each droplet evaporating at different temperatures was determined and is shown in Figure 10 (Table 2).

We incorporated the evaporation flux model proposed in this study as an interface condition in a typical computational model that analyzed fluid flow and heat transfer in and around the droplet. The objective here was to show that our model could predict the evaporation flux observed in experiments conducted at different droplet heating rates. The model geometry included the ceramic heater (rather than the QCM), which influenced the flow around the droplets. Further, the power delivered to the heater (Table 2) was included in the model as a heat

source to obtain the experimentally measured heater temperature. The evaporation flux at the droplet-air interface was changed from Eq.(19) to Eq. (21) to prescribe the flux based on a given AC and the local temperature of the liquid-vapor interface. The derivation of this boundary condition can also be found in the supplementary material. The remaining boundary conditions and governing equations are identical to the computational model used to determine the AC (Section 2.3).

Table 2:	Validation	Experiments	Parameters
racic 2.	' unaution	Lapermients	1 didilicters

Validation Experiment	V1	V2	V3	V4
Heater Power (mW)	73	142	200	279
Heater Temperature (°C)	29	35	40	46
Initial Droplet Volume (mm ³)	3.19	3.56	2.96	2.88
Initial Contact Angle (°)	79.9	78.1	70.5	69.7
Total Evaporation time (s)	589	427	292	191
Time Segment Length (s)	100	80	60	40

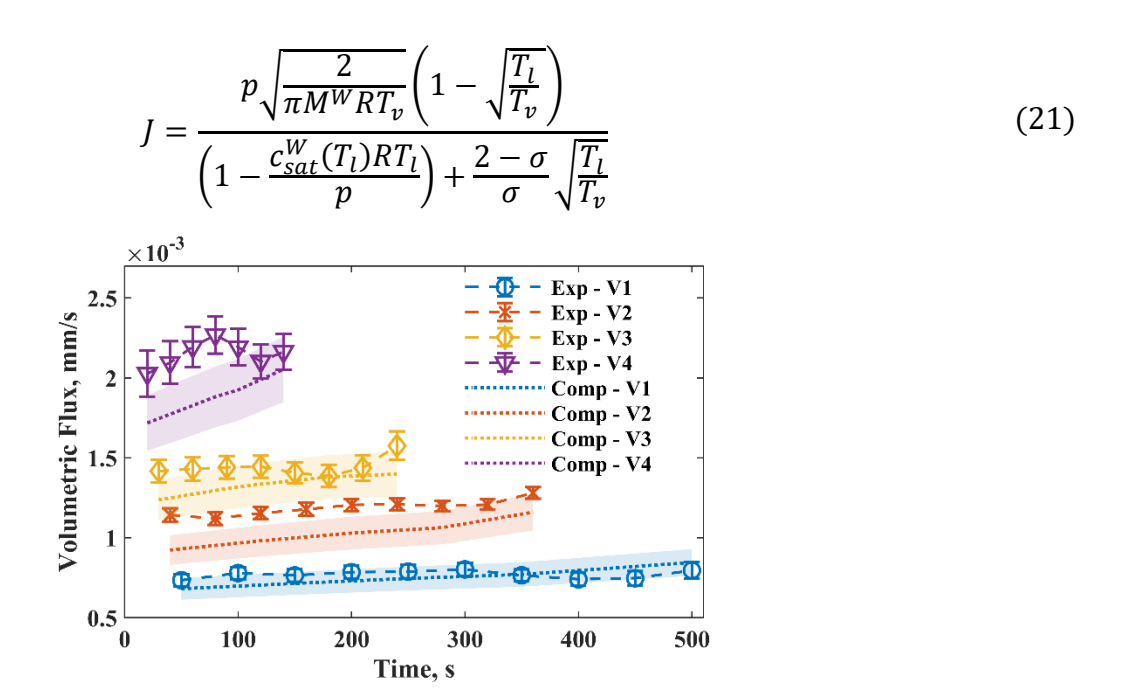


Figure 10. Volumetric flux over time for each validation experiment (Table 2) compared with the computational prediction using Eq. (21) as the interface flux condition with $\sigma = 0.001 \pm 0.0001$. Uncertainty in the computational result was determined by sensitivity analysis to the AC value and is shown as a colored band.

Figure 10 compares the volumetric flux from the model and experiments. The results from the computational model align well with the experimental results, with their error bars overlapping for each data. This figure illustrates the accuracy of the predicted evaporation flux using a conventional computational model that assumes an AC of $\sigma = 0.001 \pm 0.0001$, which results in the spread shown in Figure 10. The discrepancy in the initial few seconds of droplet evaporation, wherein the computational prediction is lower than experimental measurements

for some droplets, is due to the model not accounting for flow inside the droplet, which would promote evaporation by increasing the interface temperature. However, at later stages involving decreased droplet heights, internal flow is more restricted, and consequently, the impact of not including it in the model becomes minimal. The sensitivity and uncertainty analysis of the data in Figure 10 can be found in the supplementary material.

In summary, predicting the performance of phase change devices is inherently challenging since several factors affect evaporation flux. Well formulated kinetic theory of gasses, such as Schrage's analysis, ⁴³ describes evaporation at the liquid-vapor interface. However, the AC for water-containing systems can vary over orders of magnitude²⁰ and should be considered a material-dependent property. In many applications, such as those of air-water systems, the accumulation of impurities, both solid and non-condensable gasses, are unavoidable, and an AC of unity should not be used to predict device performance. In binary systems such as this work, the correct formulation of the kinetic theory of gasses can be used to predict device performance (Eqs. (6) and (7)) with a known AC. For air-water systems comparable to this work, such as evaporative cooling by jet impingement, ⁵⁵ desalination, ^{8,56} and water harvesting, ⁵⁹ an AC value of 0.001 could be used to predict performance. This simple flux model yields good agreement with the experiments and that the AC value of 0.001 is correct and usable.

4 Conclusion

Evaporation is an essential phenomenon in many applications and understanding the influence of various factors on evaporation dynamics is crucial. This study performs a coupled experimental-computational analysis of sessile droplet evaporation of nominally pure water of various sizes (2-4 µL) evaporating into a low-speed dry nitrogen stream in an enclosed humidity-controlled chamber. High-precision experimental measurements using a QCM as an instantaneous radius sensor was combined with multi-scale computational analysis considering the Knudsen layer's concentration and temperature jumps to elucidate relationships between factors affecting the evaporation dynamics of sessile droplets, including determining the accommodation coefficient in Schrage's binary gas relationships (Eqs. (6) and (7)) involving a non-condensable gas.

This work finds the surface-averaged accommodation coefficient to be close to 0.001 for pure water droplets evaporating into a near-pure nitrogen environment at atmospheric pressure. While this value is low compared to a theoretical maximum of unity, it is not without precedent. The presence of non-condensable gas has been previously shown to reduce accommodation coefficients in numerical and theoretical works. Additionally, the surface-averaged accommodation coefficient's value is nearly constant during evaporation, even as the evaporative flux changes with time.

Furthermore, each nominally pure water droplet analyzed in this study contained some trace non-volatile impurities that created an annular residue onto the QCM at the end of evaporation. For these droplets, while the deposited impurity mass was less than 100 ng (32 ppm), it influenced the evaporation rate, and thus the accommodation coefficient, seen most clearly in Droplet 3 (Figure 9), where the accommodation coefficient decreases markedly at the end of evaporation as the non-volatile impurities increase in concentration. It is particularly challenging to maintain deionized water in a pristine condition, and trace impurities cannot be measured easily using traditional methods (*e.g.*, imaging, mass-balance). Hence, the presence of impurities is seldom reported. However, this study shows, for the first time, that QCM can measure trace impurities during evaporation. We believe further research can elucidate the effect of non-volatile impurities on evaporation kinetics.

The evaporation flux was found to vary significantly over the liquid-vapor interface. Besides the vapor pressure and temperature distribution across the droplet surface, the flux distribution depends on the accommodation coefficient. For applications involving the evaporation of liquids into a non-condensable medium, we believe that the novel approach presented in this study involving the combined experimental-numerical technique can help determine the accommodation coefficients in the interfacial evaporation flux relationships. This technique is advantageous in applications where it is challenging to quantify interfacial quantities, such as temperature and vapor concentration, to predict evaporation kinetics.

5 Acknowledgments

The work was supported by the National Science Foundation's Division of Chemical, Bioengineering, Environmental, and Transport Systems in the Directorate for Engineering under Grant No. 1944323.

6 References

- (1) Maxwell, J. C.; Niven, W. D. *The Scientific Papers of James Clerk Maxwell*; University Press, 2011; Vol. 2. https://doi.org/10.1017/CBO9780511710377.
- (2) Langmuir, I. The Evaporation of Small Spheres. *Phys. Rev.* **1918**, *12* (5), 368–370. https://doi.org/10.1103/PhysRev.12.368.
- (3) Sazhin, S. S. Advanced Models of Fuel Droplet Heating and Evaporation. *Prog. Energy Combust. Sci.* **2006**, *32* (2), 162–214. https://doi.org/10.1016/j.pecs.2005.11.001.
- (4) Kryukov, A. P.; Levashov, V. Y.; Sazhin, S. S. Evaporation of Diesel Fuel Droplets: Kinetic versus Hydrodynamic Models. *Int. J. Heat Mass Transf.* **2004**, *47* (12–13), 2541–2549. https://doi.org/10.1016/j.ijheatmasstransfer.2004.01.004.
- (5) Erbil, H. Y. Evaporation of Pure Liquid Sessile and Spherical Suspended Drops: A Review. *Adv. Colloid Interface Sci.* **2012**, *170* (1–2), 67–86. https://doi.org/10.1016/j.cis.2011.12.006.
- Walker, G. M.; Beebe, D. J. An Evaporation-Based Microfluidic Sample Concentration Method. *Lab Chip* **2002**, *2* (2), 57–61. https://doi.org/10.1039/b202473j.
- (7) Nie, C.; Frijns, A. J. H.; Mandamparambil, R.; den Toonder, J. M. J. A Microfluidic Device Based on an Evaporation-Driven Micropump. *Biomed. Microdevices* **2015**, *17* (2). https://doi.org/10.1007/s10544-015-9948-7.
- (8) El-Dessouky, H. T.; Ettouney, H. M. Multiple-Effect Evaporation Desalination Systems: Thermal Analysis. *Desalination* **1999**, *125* (1–3), 259–276. https://doi.org/10.1016/S0011-9164(99)00147-2.
- (9) Gleason, K.; Putnam, S. A. Microdroplet Evaporation with a Forced Pinned Contact Line. *Langmuir* **2014**, 30 (34), 10548–10555. https://doi.org/10.1021/la501770g.
- (10) Chandra, S.; Di Marzo, M.; Qiao, Y. M.; Tartarini, P. Effect of Liquid-Solid Contact Angle on Droplet Evaporation. *Fire Saf. J.* **1996**, *27* (2), 141–158. https://doi.org/10.1016/S0379-7112(96)00040-9.
- (11) Zang, D.; Tarafdar, S.; Tarasevich, Y. Y.; Dutta Choudhury, M.; Dutta, T. Evaporation of a Droplet: From Physics to Applications. *Phys. Rep.* **2019**, *804*, 1–56. https://doi.org/10.1016/j.physrep.2019.01.008.
- (12) Narayanan, S.; Fedorov, A. G.; Joshi, Y. K. Gas-Assisted Thin-Film Evaporation from Confined Spaces for Dissipation of High Heat Fluxes. *Nanoscale Microscale Thermophys. Eng.* **2009**, *13* (1), 30–53. https://doi.org/10.1080/15567260802625908.
- (13) Weibel, J. A.; Garimella, S. V.; North, M. T. Characterization of Evaporation and Boiling from Sintered Powder Wicks Fed by Capillary Action. *Int. J. Heat Mass Transf.* **2010**, *53* (19–20), 4204–4215. https://doi.org/10.1016/j.ijheatmasstransfer.2010.05.043.
- (14) Narayanan, S.; Fedorov, A. G.; Joshi, Y. K. Interfacial Transport of Evaporating Water Confined in Nanopores. *Langmuir* **2011**, *27* (17), 10666–10676. https://doi.org/10.1021/la201807a.
- (15) Xiao, R.; Maroo, S. C.; Wang, E. N. Negative Pressures in Nanoporous Membranes for Thin Film Evaporation. *Appl. Phys. Lett.* **2013**, *102* (12), 123103. https://doi.org/10.1063/1.4798243.
- (16) Sircar, J. D.; Hanks, D. F.; Lu, Z.; Salamon, T.; Bagnall, K. R.; Narayanan, S.; Antao, D.; Barabadi, B.; Wang, E. N. High Heat Flux Evaporation from Nanoporous Silicon Membranes. In *Proceedings of the 16th InterSociety Conference on Thermal and Thermomechanical Phenomena in Electronic Systems*,

- ITherm 2017; 2017; pp 505–513. https://doi.org/10.1109/ITHERM.2017.7992516.
- (17) Lu, Z.; Kinefuchi, I.; Wilke, K. L.; Vaartstra, G.; Wang, E. N. A Unified Relationship for Evaporation Kinetics at Low Mach Numbers. *Nat. Commun.* **2019**, *10* (1). https://doi.org/10.1038/s41467-019-10209-w.
- (18) Lu, Z.; Salamon, T. R.; Narayanan, S.; Bagnall, K. R.; Hanks, D. F.; Antao, D. S.; Barabadi, B.; Sircar, J.; Simon, M. E.; Wang, E. N. Design and Modeling of Membrane-Based Evaporative Cooling Devices for Thermal Management of High Heat Fluxes. *IEEE Trans. Components, Packag. Manuf. Technol.* **2016**, *6* (7), 1058–1067. https://doi.org/10.1109/TCPMT.2016.2576998.
- (19) Narayanan, S.; Fedorov, A. G.; Joshi, Y. K. On-Chip Thermal Management of Hotspots Using a Perspiration Nanopatch. *J. Micromechanics Microengineering* **2010**, *20* (7). https://doi.org/10.1088/0960-1317/20/7/075010.
- (20) Marek, R.; Straub, J. Analysis of the Evaporation Coefficient and the Condensation Coefficient of Water. *Int. J. Heat Mass Transf.* **2001**, *44* (1), 39–53. https://doi.org/10.1016/S0017-9310(00)00086-7.
- (21) Eames, I. W.; Marr, N. J.; Sabir, H. The Evaporation Coefficient of Water: A Review. *Int. J. Heat Mass Transf.* **1997**, *40* (12), 2963–2973. https://doi.org/10.1016/S0017-9310(96)00339-0.
- (22) Smith, J. D.; Cappa, C. D.; Drisdell, W. S.; Cohen, R. C.; Saykally, R. J. Raman Thermometry Measurements of Free Evaporation from Liquid Water Droplets. *J. Am. Chem. Soc.* **2006**, *128* (39), 12892–12898. https://doi.org/10.1021/ja063579v.
- (23) Su, Y.; Wang, W.; Wang, W.; Zhai, L.; Shen, X.; Xu, J.; Li, Z. Evaluation of Mass Accommodation Coefficients of Water over a Wide Temperature Range and Determination of Diffusion Coefficient of Water in Nitrogen. *Int. J. Thermophys.* **2021**, *42* (4). https://doi.org/10.1007/s10765-021-02795-z.
- (24) Akkus, Y.; Gurer, A. T.; Bellur, K. Drifting Mass Accommodation Coefficients: In Situ Measurements from a Steady State Molecular Dynamics Setup. **2020**, 1–32.
- (25) Persad, A. H.; Ward, C. A. Expressions for the Evaporation and Condensation Coefficients in the Hertz-Knudsen Relation. *Chem. Rev.* **2016**, *116* (14), 7727–7767. https://doi.org/10.1021/acs.chemrev.5b00511.
- (26) Gatapova, E. Y.; Graur, I. A.; Kabov, O. A.; Aniskin, V. M.; Filipenko, M. A.; Sharipov, F.; Tadrist, L. The Temperature Jump at Water Air Interface during Evaporation. *Int. J. Heat Mass Transf.* **2017**, *104*, 800–812. https://doi.org/10.1016/j.ijheatmasstransfer.2016.08.111.
- (27) Sobac, B.; Brutin, D. Thermal Effects of the Substrate on Water Droplet Evaporation. *Phys. Rev. E Stat. Nonlinear, Soft Matter Phys.* **2012**, *86* (2), 1–10. https://doi.org/10.1103/PhysRevE.86.021602.
- (28) Brutin, D.; Starov, V. Recent Advances in Droplet Wetting and Evaporation. *Chem. Soc. Rev.* **2018**, 47 (2), 558–585. https://doi.org/10.1039/c6cs00902f.
- (29) Picknett, R. G.; Bexon, R. The Evaporation of Sessile or Pendant Drops in Still Air. *J. Colloid Interface Sci.* **1977**, *61* (2), 336–350. https://doi.org/10.1016/0021-9797(77)90396-4.
- (30) Hu, H.; Larson, R. G. Evaporation of a Sessile Droplet on a Substrate. *J. Phys. Chem. B* **2002**, *106* (6), 1334–1344. https://doi.org/10.1021/jp0118322.
- (31) Deegan, R. D.; Bakajin, O.; Dupont, T. F.; Huber, G.; Nagel, S. R.; Witten, T. A. Contact Line Deposits in an Evaporating Drop. *Phys. Rev. E Stat. Physics, Plasmas, Fluids, Relat. Interdiscip. Top.* **2000**, *62* (1 B), 756–765. https://doi.org/10.1103/PhysRevE.62.756.
- (32) Hu, H.; Larson, R. G. Marangoni Effect Reverses Coffee-Ring Depositions. *J. Phys. Chem. B* **2006**, *110* (14), 7090–7094. https://doi.org/10.1021/jp0609232.

- (33) Deegan, R. D.; Bakajin, O.; Dupont, T. F.; Huber, G.; Nagel, S. R.; Witten, T. A. Capillary Flow as the Cause of Ring Stains from Dried Liquid Drops. *Nature* **1997**, *389* (6653), 827–829. https://doi.org/10.1038/39827.
- (34) Popov, Y. O. Evaporative Deposition Patterns: Spatial Dimensions of the Deposit; 2005; Vol. 71. https://doi.org/10.1103/PhysRevE.71.036313.
- (35) Sefiane, K.; Wilson, S. K.; David, S.; Dunn, G. J.; Duffy, B. R. On the Effect of the Atmosphere on the Evaporation of Sessile Droplets of Water. *Phys. Fluids* **2009**, *21* (6), 21. https://doi.org/10.1063/1.3131062.
- (36) Carrier, O.; Shahidzadeh-Bonn, N.; Zargar, R.; Aytouna, M.; Habibi, M.; Eggers, J.; Bonn, D. Evaporation of Water: Evaporation Rate and Collective Effects. *J. Fluid Mech.* **2016**, 798, 774–786. https://doi.org/10.1017/jfm.2016.356.
- (37) Poulard, C.; Guéna, G.; Cazabat, A. M. Diffusion-Driven Evaporation of Sessile Drops. *J. Phys. Condens. Matter* **2005**, *17* (49). https://doi.org/10.1088/0953-8984/17/49/015.
- (38) Cazabat, A. M.; Guéna, G. Evaporation of Macroscopic Sessile Droplets. *Soft Matter*. 2010, pp 2591–2612. https://doi.org/10.1039/b924477h.
- (39) Birdi, K. S.; Vu, D. T.; Winter, A. A Study of the Evaporation Rates of Small Water Drops Placed on a Solid Surface. *J. Phys. Chem.* **1989**, *93* (9), 3702–3703. https://doi.org/10.1021/j100346a065.
- (40) Dunn, G. J.; Wilson, S. K.; Duffy, B. R.; David, S.; Sefiane, K. The Strong Influence of Substrate Conductivity on Droplet Evaporation. *J. Fluid Mech.* **2009**, *623*, 329–351. https://doi.org/10.1017/S0022112008005004.
- (41) Dunn, G. J.; Wilson, S. K.; Duffy, B. R.; David, S.; Sefiane, K. A Mathematical Model for the Evaporation of a Thin Sessile Liquid Droplet: Comparison between Experiment and Theory. *Colloids Surfaces A Physicochem. Eng. Asp.* **2008**, *323* (1–3), 50–55. https://doi.org/10.1016/j.colsurfa.2007.09.031.
- (42) Bird, E.; Liang, Z. Transport Phenomena in the Knudsen Layer near an Evaporating Surface. *Phys. Rev. E* **2019**, *100* (4), 43108. https://doi.org/10.1103/PhysRevE.100.043108.
- (43) Schrage, R. W. A Theoretical Study of Interphase Mass Transfer; Columbia University Press: New York, 1953.
- (44) Ytrehus, T.; Østmo, S. Kinetic Theory Approach to Interphase Processes. *Int. J. Multiph. Flow* **1996**, *22* (1), 133–155. https://doi.org/10.1016/0301-9322(95)00056-9.
- (45) Sone, Y. Kinetic Theoretical Studies of the Half-Space Problem of Evaporation and Condensation. *Transp. Theory Stat. Phys.* **2000**, *29* (3–5), 227–260. https://doi.org/10.1080/00411450008205874.
- (46) Labuntsov, D. A.; Kryukov, A. P. Analysis of Intensive Evaporation and Condensation. *Int. J. Heat Mass Transf.* **1979**, *22* (7), 989–1002. https://doi.org/10.1016/0017-9310(79)90172-8.
- (47) Gusarov, A. V.; Smurov, I. Gas-Dynamic Boundary Conditions of Evaporation and Condensation: Numerical Analysis of the Knudsen Layer. *Phys. Fluids* **2002**, *14* (12), 4242–4255. https://doi.org/10.1063/1.1516211.
- (48) Fischer, J. Distribution of Pure Vapor between Two Parallel Plates under the Influence of Strong Evaporation and Condensation. *Phys. Fluids* **1976**, *19* (9), 1305–1311.
- (49) Sibold, D.; Urbassek, H. M. Monte Carlo Study of Knudsen Layers in Evaporation from Elemental and Binary Media. *Phys. Fluids A* **1993**, *5* (1), 243–256. https://doi.org/10.1063/1.858779.
- (50) Liang, Z.; Keblinski, P. Molecular Simulation of Steady-State Evaporation and Condensation in the Presence of a Non-Condensable Gas. *J. Chem. Phys.* **2018**, *148* (6), 64708.

- https://doi.org/10.1063/1.5020095.
- (51) Liang, Z.; Chandra, A.; Bird, E.; Keblinski, P. A Molecular Dynamics Study of Transient Evaporation and Condensation. *Int. J. Heat Mass Transf.* **2020**, *149*, 119152. https://doi.org/10.1016/j.ijheatmasstransfer.2019.119152.
- (52) Nie, J.; Chandra, A.; Liang, Z.; Keblinski, P. Mass Accommodation at a High-Velocity Water Liquid-Vapor Interface. *J. Chem. Phys.* **2019**, *150* (15), 154705. https://doi.org/10.1063/1.5091724.
- (53) Liang, Z.; Biben, T.; Keblinski, P. Molecular Simulation of Steady-State Evaporation and Condensation: Validity of the Schrage Relationships. *Int. J. Heat Mass Transf.* **2017**, *114*, 105–114. https://doi.org/10.1016/j.ijheatmasstransfer.2017.06.025.
- (54) Barclay, P. L.; Lukes, J. R. Curvature Dependence of the Mass Accommodation Coefficient. *Langmuir* **2019**, *35* (18), 6196–6202. https://doi.org/10.1021/acs.langmuir.9b00537.
- (55) Narayanan, S.; Fedorov, A. G.; Joshi, Y. K. Heat and Mass Transfer during Evaporation of Thin Liquid Films Confined by Nanoporous Membranes Subjected to Air Jet Impingement. *Int. J. Heat Mass Transf.* **2013**, *58* (1–2), 300–311. https://doi.org/10.1016/j.ijheatmasstransfer.2012.11.015.
- (56) Wang, X.; Hsieh, M. L.; Bur, J. A.; Lin, S. Y.; Narayanan, S. Capillary-Driven Solar-Thermal Water Desalination Using a Porous Selective Absorber. *Mater. Today Energy* **2020**, *17*, 100453. https://doi.org/10.1016/j.mtener.2020.100453.
- (57) Narayanan, S.; Kim, H.; Umans, A.; Yang, S.; Li, X.; Schiffres, S. N.; Rao, S. R.; McKay, I. S.; Wang, E. N.; Rios Perez, C. A.; Hidrovo, C. H. A Thermophysical Battery for Storage-Based Climate Control. *Appl. Energy* **2017**, *189*, 31–43. https://doi.org/10.1016/j.apenergy.2016.12.003.
- (58) Narayanan, S.; Li, X.; Yang, S.; Kim, H.; Umans, A.; McKay, I. S.; Wang, E. N. Thermal Battery for Portable Climate Control. *Appl. Energy* **2015**, *149*, 104–116. https://doi.org/10.1016/j.apenergy.2015.03.101.
- (59) Kim, Hyunho, Yang, S.; Rao, S. R.; Narayanan, S.; Kapustin, E. A.; Furukawa, H.; Umans, A. S.; Yaghi, O. M.; Wang, E. N. Water Harvesting from Air with Metal-Organic Frameworks Powered by Natural Sunlight. *Science* (80-.). 2017, 434 (April), 430–434.
- (60) Gonzalez, J.; Ortega, J.; Liang, Z. Prediction of Thermal Conductance at Liquid-Gas Interfaces Using Molecular Dynamics Simulations. *Int. J. Heat Mass Transf.* **2018**, *126*, 1183–1192. https://doi.org/10.1016/j.ijheatmasstransfer.2018.06.088.
- (61) Kobayashi, K.; Sasaki, K.; Kon, M.; Fujii, H.; Watanabe, M. Kinetic Boundary Conditions for Vapor–Gas Binary Mixture. *Microfluid. Nanofluidics* **2017**, *21* (3), 53. https://doi.org/10.1007/s10404-017-1887-6.
- (62) Ohashi, K.; Kobayashi, K.; Fujii, H.; Watanabe, M. Evaporation Coefficient and Condensation Coefficient of Vapor under High Gas Pressure Conditions. *Sci. Rep.* **2020**, *10*, 8143. https://doi.org/10.1038/s41598-020-64905-5.
- (63) Frezzotti, A. Boundary Conditions at the Vapor-Liquid Interface. *Phys. Fluids* **2011**, *23* (3). https://doi.org/10.1063/1.3567001.
- (64) Frezzotti, A.; Gibelli, L.; Lockerby, D. A.; Sprittles, J. E. Mean-Field Kinetic Theory Approach to Evaporation of a Binary Liquid into Vacuum. *Phys. Rev. Fluids* **2018**, *3* (5), 1–17. https://doi.org/10.1103/PhysRevFluids.3.054001.
- (65) Young, J. B. The Condensation and Evaporation of Liquid Droplets at Arbitrary Knudsen Number in the Presence of an Inert Gas. *Int. J. Heat Mass Transf.* **1993**, *36* (11), 2941–2956. https://doi.org/10.1016/0017-9310(93)90112-J.

- (66) Aoki, K.; Takata, S.; Kosuge, S. Vapor Flows Caused by Evaporation and Condensation on Two Parallel Plane Surfaces: Effect of the Presence of a Noncondensable Gas. *Phys. Fluids* **1998**, *10* (6), 1519–1533.
- (67) Frezzotti, A.; Ytrehus, T. Kinetic Theory Study of Steady Condensation of a Polyatomic Gas. *Phys. Fluids* **2006**, *18* (2), 27101. https://doi.org/10.1063/1.2171231.
- (68) Murisic, N.; Kondic, L. On Evaporation of Sessile Drops with Moving Contact Lines. *J. Fluid Mech.* **2011**, 679, 219–246. https://doi.org/10.1017/jfm.2011.133.
- (69) Hertz, H. Ueber Die Berührung Fester Elastischer Körper. *J. für die reine und Angew. Math.* **1882**, *1882* (92), 156–171.
- (70) Knudsen, M. Die Maximale Verdampfungsgeschwindigkeit Des Quecksilbers. *Ann. Phys.* **1915**, *352* (13), 697–708. https://doi.org/10.1002/andp.19153521306.
- (71) Aursand, E.; Ytrehus, T. Comparison of Kinetic Theory Evaporation Models for Liquid Thin-Films. *Int. J. Multiph. Flow* **2019**, *116*, 67–79. https://doi.org/10.1016/j.ijmultiphaseflow.2019.04.007.
- (72) Rumble, J. R. ed. *Handbook of Chemistry and Physics 100th Edition*, 100th ed.; Rumble, J., Ed.; CRC Press: Boca Raton, FL, 2019. https://doi.org/10.1007/978-3-642-14998-6_4.
- (73) Murray, B.; Narayanan, S. The Role of Wettability on the Response of a Quartz Crystal Microbalance Loaded with a Sessile Droplet. *Sci. Rep.* **2019**, *9* (1), 1–13. https://doi.org/10.1038/s41598-019-53233-y.
- (74) Murray, B.; Fox, M. J.; Narayanan, S. Quantifying the Evaporation Rate of Sessile Droplets Using a Quartz Crystal Microbalance. *J. Appl. Phys.* **2020**, *128* (3), 035101. https://doi.org/10.1063/5.0005239.
- (75) Zhuang, H.; Lu, P.; Lim, S. P.; Lee, H. P. Study of the Evaporation of Colloidal Suspension Droplets with the Quartz Crystal Microbalance. *Langmuir* **2008**, *24* (15), 8373–8378. https://doi.org/10.1021/la800661g.
- (76) Couturier, G.; Vatinel, S.; Boisgard, R.; Aim, J. P.; Chabli, A. Quartz Crystal Microbalance and Evaporation of Sessile Droplets. *J. Appl. Phys.* **2009**, *106* (5), 054906. https://doi.org/10.1063/1.3204661.
- (77) Pham, N. T.; McHale, G.; Newton, M. I.; Carroll, B. J.; Rowan, S. M. Application of the Quartz Crystal Microbalance to the Evaporation of Colloidal Suspension Droplets. *Langmuir* **2004**, *20* (3), 841–847. https://doi.org/10.1021/la0357007.
- (78) Joyce, M. J.; Todaro, P.; Penfold, R.; Port, S. N.; May, J. A. W.; Barnes, C.; Peyton, A. J. Evaporation of Sessile Drops: Application of the Quartz Crystal Microbalance. *Langmuir* **2000**, *16* (8), 4024–4033. https://doi.org/10.1021/la9906601.
- (79) Lee, M.; Kim, W.; Lee, S.; Baek, S.; Yong, K.; Jeon, S. Water Droplet Evaporation from Sticky Superhydrophobic Surfaces. *Appl. Phys. Lett.* **2017**, *111* (2). https://doi.org/10.1063/1.4992140.
- (80) Lin, Z.; Ward, M. D. Determination of Contact Angles and Surface Tension with the Quartz Crystal Microbalance. *Anal. Chem.* **1996**, *68* (8), 1285–1291. https://doi.org/10.1021/ac951131z.
- (81) Zhuang, H.; Lu, P.; Lim, S. P.; Lee, H. P. Frequency Response of a Quartz Crystal Microbalance Loaded by Liquid Drops. *Langmuir* **2007**, *23* (13), 7392–7397. https://doi.org/10.1021/la063767z.
- (82) Lin, Z.; Stoebe, T.; Hill, R. M.; Davis, H. T.; Ward, M. D. Improved Accuracy in Dynamic Quartz Crystal Microbalance Measurements of Surfactant Enhanced Spreading. *Langmuir* **1996**, *12* (2), 345–347. https://doi.org/10.1021/la950514p.
- (83) Lin, J. W.; Fan, S. K. Real Time Contact Angle Measurement by Quartz Crystal Microbalance for EWOD Studies. 2010 IEEE 5th Int. Conf. Nano/Micro Eng. Mol. Syst. NEMS 2010 2010, No. 3, 325–328. https://doi.org/10.1109/NEMS.2010.5592230.
- (84) Esmeryan, K. D.; McHale, G.; Trabi, C. L.; Geraldi, N. R.; Newton, M. I. Manipulated Wettability of a

- Superhydrophobic Quartz Crystal Microbalance through Electrowetting. *J. Phys. D. Appl. Phys.* **2013**, *46* (34), 1–9. https://doi.org/10.1088/0022-3727/46/34/345307.
- (85) Kwon, S. Y.; Kim, J. C.; Choi, B. Il. Recognition of Supercooled Dew in a Quartz Crystal Microbalance Dew-Point Sensor by Slip Phenomena. *Metrologia* **2007**, *44* (5), L37–L40. https://doi.org/10.1088/0026-1394/44/5/N01.
- (86) Xue, Y.; Wu, Y.; Pei, X.; Duan, H.; Xue, Q.; Zhou, F. How Solid-Liquid Adhesive Property Regulates Liquid Slippage on Solid Surfaces? *Langmuir* **2015**, *31* (1), 226–232. https://doi.org/10.1021/la503972m.
- (87) Zhuang, H.; Lu, P.; Siak, P. L.; Heow, P. L. Effects of Interface Slip and Viscoelasticity on the Dynamic Response of Droplet Quartz Crystal Microbalances. *Anal. Chem.* **2008**, *80* (19), 7347–7353. https://doi.org/10.1021/ac8010523.
- (88) Zhuang, H.; Lim, S. P.; Lee, H. P. Effects of Compressional Waves on the Response of Quartz Crystal Microbalance in Contact with Silicone Oil Droplets. *J. Appl. Phys.* **2009**, *105* (11), 1993. https://doi.org/10.1063/1.3133144.
- (89) Zhuang, H.; Lee, H. P.; Lim, S. P. Dynamic Response of Quartz Crystal Microbalances in Contact with Silicone Oil Droplets. In *Fourth International Conference on Experimental Mechanics*; Quan, C., Qian, K., Asundi, A. K., Chau, F. S., Eds.; 2009; Vol. 7522, p 75222X. https://doi.org/10.1117/12.848916.
- (90) McHale, G.; Roach, P.; Evans, C. R.; Shirtcliffe, N. J.; Elliott, S. J.; Newton, M. I. Sensor Response of Superhydrophobic Quartz Crystal Resonators. In *2008 IEEE International Frequency Control Symposium*, *FCS*; IEEE, 2008; pp 698–704. https://doi.org/10.1109/FREQ.2008.4623089.
- (91) Roach, P.; McHale, G.; Evans, C. R.; Shirtcliffe, N. J.; Newton, M. I. Decoupling of the Liquid Response of a Superhydrophobic Quartz Crystal Microbalance. *Langmuir* **2007**, *23* (19), 9823–9830. https://doi.org/10.1021/la701089a.
- (92) Pye, J. E.; Wood, C. E.; Burton, J. C. Precursors to Molecular Slip on Smooth Hydrophobic Surfaces. *Phys. Rev. Lett.* **2018**, *121* (13). https://doi.org/10.1103/PhysRevLett.121.134501.
- (93) Su, J.; Charmchi, M.; Sun, H. A Study of Drop-Microstructured Surface Interactions during Dropwise Condensation with Quartz Crystal Microbalance. *Sci. Rep.* **2016**, *6* (September), 1–11. https://doi.org/10.1038/srep35132.
- (94) Ash, D. C.; Joyce, M. J.; Barnes, C.; Booth, C. J.; Jefferies, A. C. Viscosity Measurement of Industrial Oils Using the Droplet Quartz Crystal Microbalance. *Meas. Sci. Technol.* **2003**, *14* (11), 1955–1962. https://doi.org/10.1088/0957-0233/14/11/013.
- (95) Bai, Q.; Hu, J.; Huang, X.; Huang, H. Using QCM for Field Measurement of Liquid Viscosities in a Novel Mass-Sensitivity-Base Method. In 2016 IEEE International Frequency Control Symposium, IFCS 2016 Proceedings; IEEE: New Orleans, LA, USA, 2016; pp 1–3. https://doi.org/10.1109/FCS.2016.7546819.
- (96) Lin, Z.; Hill, R. M.; Davis, H. T.; Ward, M. D. Determination of Wetting Velocities of Surfactant Superspreaders with the Quartz Crystal Microbalance. *Langmuir* **1994**, *10* (11), 4060–4068. https://doi.org/10.1021/la00023a026.
- (97) Lin, Z.; Ward, M. D. The Role of Longitudinal Waves in Quartz Crystal Microbalance Applications in Liquids. *Anal. Chem.* **1995**, *67* (4), 685–693. https://doi.org/10.1021/ac00100a001.
- (98) Hillier, A. C.; Ward, M. D. Scanning Electrochemical Mass Sensitivity Mapping of the Quartz Crystal Microbalance in Liquid Media. *Anal. Chem.* **1992**, *64* (21), 2539–2554. https://doi.org/10.1021/ac00045a014.
- (99) COMSOL AB, S. COMSOL Multiphysics ® v. 5.5. COMSOL AB: Stockholm, Sweden 2019.

- (100) Girard, F.; Antoni, M.; Sefiane, K. On the Effect of Marangoni Flow on Evaporation Rates of Heated Water Drops. *Langmuir* **2008**, *24* (17), 9207–9210. https://doi.org/10.1021/la801294x.
- (101) York, D.; Evensen, N. M.; Martínez, M. L.; De Basabe Delgado, J. Unified Equations for the Slope, Intercept, and Standard Errors of the Best Straight Line. *Am. J. Phys.* **2004**, *72* (3), 367–375. https://doi.org/10.1119/1.1632486.